Spin-dependent low-energy electron transport in metals

B. Solleder,[1] C. Lemell,[1] K. Tőkési,[2] N. Hatcher,[3] and J. Burgdörfer[1]
[1]*Institute for Theoretical Physics, Vienna University of Technology, 1040 Vienna, Austria, EU*
[2]*Institute of Nuclear Research of the Hungarian Academy of Sciences (ATOMKI), P.O. Box 51, 4001 Debrecen, Hungary, EU*
[3]*Department of Physics and Astronomy, Northwestern University, Evanston, Illinois 60208-3112, USA*
(Received 22 May 2007; published 15 August 2007)

Spin-dependent transport of low-energy electrons (⩽500 eV) through metals is studied using Monte Carlo simulations which employ collision kernels constructed from microscopic response functions and spin density of states calculated with the density functional full-potential linearized augmented plane wave method. Trajectories of electrons are simulated as sequences of stochastic elastic and inelastic scattering events including spin-dependent processes. We apply the present description to the spin-polarized electron emission induced by the interaction of an unpolarized electron beam with magnetic Fe. Good agreement with experimental data is found.

DOI: 10.1103/PhysRevB.76.075115 PACS number(s): 72.25.Ba, 79.20.Hx

I. INTRODUCTION

Microscopic probes of magnetic materials continue to be of considerable interest driven by both basic and applied research ranging from spintronics to improving data storage devices. Several experimental methods have evolved to probe magnetized materials. While bulk properties have been studied using photoemission[1,2] or electron spectroscopy,[3] the scattering of ion or electron beams under grazing incidence conditions allows for surface sensitive studies. Information on the underlying physical processes and material properties is extracted from the polarization of emitted radiation[4] or from the spin of emitted electrons.[3,5] Probing magnetic properties is complicated by the fact that the magnetized band structure acts back on the probe and can actively influence its properties. Such investigations, therefore, probe the interaction of the magnetized material with the projectile as much as the magnetic band structure itself. Circular dichroism of photons[6] and the spin-filter effect[7,8] for electrons are cases in point.

Microscopic simulations of electron transmission through a magnetized band structure are scarce. Most theoretical studies aiming at an interpretation of the experimental data (e.g., Refs. 9–11) reach qualitative agreement with experiment. Previous studies of spin-dependent transport have been based on semiempirical models[11,12] using free parameters which were adjusted to the experimental data. The present study attempts a description of low-energy (⩽500 eV) electron transport within the framework of Monte Carlo solutions of the Langevin equation where the stochastic forces are derived from microscopic, albeit approximate, collision kernels. One key input is a state-of-the-art calculation of the magnetized band structure. We follow the complete collision cascade which takes into account the spin and energy dependences of creation and scattering processes to obtain reliable polarization spectra for emission energies down to a few eV. At low primary energies, the average penetration and escape depth of the electrons are so low that the emission spectrum contains significant contributions from surface scattering. As the first test of the present theory, we apply this method to the polarization data by Kirschner and Koike[3] for electron scattering at a magnetized iron surface. While the primary electron beam was unpolarized, the low-energy electron emission was found to be strongly polarized. We will show that the high degree of polarization results from both the spin polarization of the occupied target band structure and inelastic spin-filter processes[13,14] prominent at low energies.

This paper is organized as follows. In Sec. II we present the theoretical framework of the present transport simulations and review the approximations used for determining the input, the collision kernels, and the band structure. In Sec. III, we present numerical results and a comparison with experimental data for low-energy (⩽500 eV) electron scattering at iron. Atomic units (a.u.) are used unless stated otherwise.

II. THEORY

A. Scenario

In our work, electron transport is treated in the framework of the classical transport theory[15] (CTT) for open systems, in which the electronic dynamics is represented by a classical phase-space distribution $f(\vec{r},\dot{\vec{r}},t)$ whose evolution is determined by test-particle discretization, i.e., by solving the corresponding Langevin equation for representative trajectories $(i=1,\ldots,N_E)$,

$$\ddot{\vec{r}}_i = -\vec{\nabla}V(\vec{r}_i,t) + \vec{F}_{stoc}(\vec{r}_i,\dot{\vec{r}}_i,t), \tag{1}$$

where N_E is the number of particles in the ensemble. The ensemble is propagated employing the classical trajectory Monte Carlo technique. The stochastic forces $\vec{F}_{stoc}$ entering Eq. (1) are derived from the collision kernels of the associated Liouville-Master equation, determined either from independent *ab initio* quantum calculations or independent experimental data. Collision processes governing the input $(\vec{F}_{stoc})$ are treated as Poissonian stochastic processes and will be discussed below in more detail. Conservative forces in Eq. (1) [i.e., $-\vec{\nabla}V(\vec{r}_i)$] will be neglected in the following but could be included straightforwardly, if needed. Two points are worth mentioning. As the stochastic forces and their un-

 ©2007 The American Physical Society

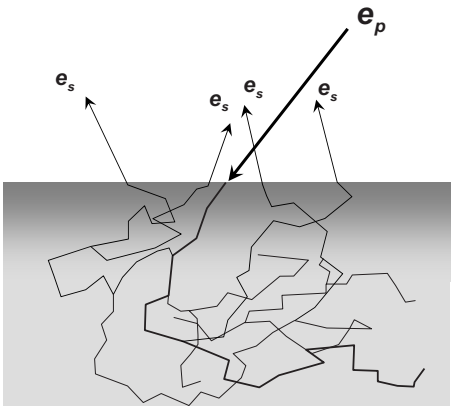

FIG. 1. Electron transport near the surface, schematically. The primary electron is denoted by e_p and escaping secondaries by e_s. The dark shaded area indicates the region where inelastic surface excitations dominate over bulk excitations.

derlying collision kernels are derivable from (mostly) quantum (linear) response functions, the resulting transport theory corresponds to a hybrid classical-quantum treatment[16] despite its purely classical appearance. In fact, in the limit $V(\vec{r}_i)=0$, the treatment is equivalent to a quantum-kinetic (Boltzmann) equation since classical-quantum correspondence holds for impulsively perturbed free-particle propagation in line with Ehrenfest's theorem. Second, the present simulation treats the entire collision cascade. Accordingly, the number of particles in the ensemble, N_E, is not constant but increases during the evolution as inelastic scattering generates secondary electrons whose trajectories are followed as well. Correlation effects between primary and secondary electrons are neglected. The spin degree of freedom is accounted for by following two subensembles of electrons with spin up and spin down which would remain decoupled in the absence of spin-dependent interactions. Spin-flip processes treated below lead to an exchange of populations among the subensembles.

Momentum, energy, and spin exchanges are simulated by a sequence of elastic and inelastic scattering events (Fig. 1). While inelastic scattering is accompanied by a certain energy loss, an elastically scattered electron is assumed to retain its energy and only momentum is transferred in the collision. Electrons are elastically scattered at the screened Coulomb potential of the atomic cores in the solid, approximated by a muffin-tin potential. Inelastic scattering proceeds by excitations of the electronic system of the solid. The negative electron charge brought into the medium constitutes a strong perturbation to the electron gas of the solid. The target electrons react by collective excitations (i.e., plasmons), by particle-hole pair creation, or by driving interband transitions. If the energy transfer suffices to raise the excited electron into an unbound state, the trajectory of this secondary electron is followed. Electrons dissipate their energy continuously until they are stopped in the bulk or escape into the vacuum. We assume that all plasmon excitations eventually decay into electron-hole pairs, thereby creating secondary electrons. Alternative relaxation channels via emission of phonons or photons are neglected. While this approximation overestimates the total electron emission, we expect this error to be of minor importance as plasmon decay into electron-hole pairs happens on a femtosecond time scale, thereby dominating over the other decay channels which typically happen on a picosecond or even larger time scale. A possible spin dependence of plasmon decay will be discussed in Sec. III.

Due to the breaking of symmetry at the solid-vacuum interface, additional excitation channels open in the vicinity of the surface. These surface excitations are dominant close to the surface (indicated by the dark shaded area in Fig. 1), while bulk excitations dominate a few a.u. below.

The stochastic force entering Eq. (1) is described as a sequence of impulsive momentum transfers $\vec{p}_{i,\alpha}$,[15]

$$\vec{F}_{stoc}(t) = \sum_{i,\alpha} \delta(t - t_i^{(\alpha)}) \Delta\vec{p}_{i,\alpha}, \tag{2}$$

where the index α labels the different channels for collision processes (elastic, inelastic, etc., see below) while the index i refers to different collisions of the same channel. The mean free path (MFP) between two collisions, λ_α, determines the time interval between two collisions,

$$\langle t_{i+1}^{(\alpha)} - t_i^{(\alpha)} \rangle = \lambda_\alpha(E_e)/v_e, \tag{3}$$

where E_e and v_e are the energy and velocity along the trajectory, respectively. The MFP is related to the collision kernel P_α (or differential scattering cross section) for each channel as

$$\lambda_\alpha^{-1} = \int d^3(\Delta p) P_\alpha(\Delta\vec{p}, E_e, s), \tag{4}$$

which may depend on the electron energy, the spin s, and, possibly, other variables as well. In Eq. (4), the integral extends over all allowed momentum transfers, consistent with energy and momentum conservation, as well as the Pauli principle of maximal single occupancy of any initial and final spin orbitals accessible by a momentum transfer $\Delta\vec{p}$. The inverse MFP [Eq. (4)] is the zeroth moment of P_α. The probability for a stochastic momentum transfer $\Delta\vec{p}_\alpha$ is given by the (normalized) kernel P_α. Accordingly, $\langle\Delta\vec{p}_\alpha\rangle$ gives the first moment of P_α. Straggling and fluctuations reflect higher moments. The total mean free path λ_{tot} is determined by the cross sections of the different scattering processes,

$$\lambda_{tot}^{-1} = \sum_\alpha \lambda_\alpha^{-1}, \tag{5}$$

and $\lambda_\alpha^{-1}/\lambda_{\text{tot}}^{-1}$ is the probability for the process α to happen. The detailed models for calculating the different λ_α are presented in the following sections.

B. Spin-polarized density of states

One key ingredient of our simulation is the magnetized band structure. The occupied states determine the initial conditions for the spin-polarized subensembles of secondary electrons as the density of occupied states constitutes, up to a normalization factor, the distribution of electron energies in the conduction band. In addition, the probability for a certain spin direction is given by the relative fraction of states of this

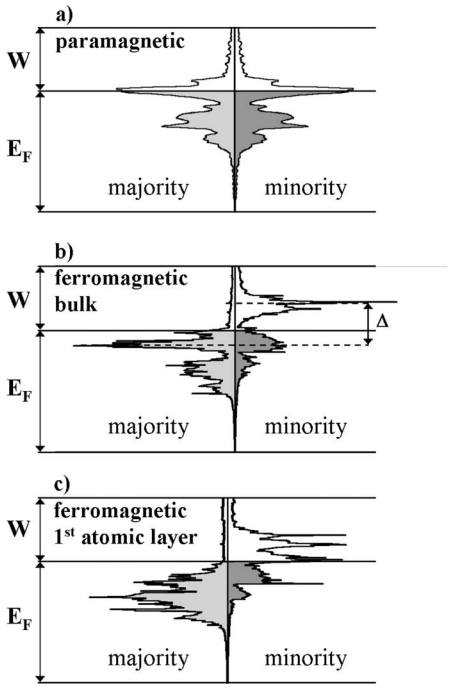

FIG. 2. SDOS for (a) paramagnetic, (b) ferromagnetic bulk, and (c) ferromagnetic surface Fe. The magnetic SDOS is characterized by an energy shift Δ between minority and majority states.

spin at the given energy. Here, the bulk spin density of states (SDOS) is used for excitations in the bulk while the SDOS of the first atomic layer is used for secondary electrons generated by surface excitations. Moreover, the unoccupied states play a key role in terms of accessible final states in inelastic scattering processes. Magnetized materials are characterized by a difference in the number of spin-up (↑) and spin-down (↓) electrons, where spin up (majority) means parallel and spin down (minority) means antiparallel to the direction of magnetization. The minority states are shifted upward in energy with respect to the majority states by the exchange splitting Δ [compare Fig. 2(b) with the paramagnetic case in Fig. 2(a)]. This leads to an excess of occupied spin-up states and, consequently, to a positive mean polarization of its electrons. The polarization P is defined as $P=(N_{\uparrow}-N_{\downarrow})/(N_{\uparrow}+N_{\downarrow})$, where $N_{\uparrow(\downarrow)}$ is the number of spin-up (down) electrons. As electrons excited from the band reflect this SDOS, secondary electrons emitted after impact of an unpolarized electron beam show a positive polarization. For very low electron energies (<15 eV), this effect is additionally enhanced by so-called Stoner excitations,[13,14] a consequence of the excess of minority spin states in the unoccupied part of the conduction band (see Sec. II F).

The present SDOS for iron was calculated using the all-electron full-potential linearized augmented plane wave method[17] in both the bulk and single slab modes. This is a fully *ab initio* density functional theory implementation that uses the Perdew-Burke-Ernzerhof generalized gradient approximation[18] exchange-correlation potential with 66 k points. Cutoffs to the plane wave basis (0.49 a.u.) and the potential representation (1.32 a.u.), and spherical harmonics with $l \leqslant 8$ were used in achieving self-consistency. The spin-dependent electronic structure of the seven layer Fe(001) thin film and bulk Fe bcc was determined after structural relaxation. The SDOS in Fig. 2 is shown for the spin-polarized (ferromagnetic) and non-spin-polarized (paramagnetic) calculations.

C. Elastic scattering

An electron traveling through a solid medium is elastically scattered off the screened core potentials of the lattice atoms. The elastic ($\alpha=e$) mean free path (EMFP) λ_e between subsequent elastic scattering events depends on the atomic density ρ of the solid and the total elastic scattering cross section σ_e and is given by $\lambda_e=1/(\rho\sigma_e)$. The momentum transfer in an elastic scattering process depends on the scattering angle θ, which is determined by the collision kernel for elastic scattering, i.e., the differential cross section $d\sigma_e/d\Omega$. As we study spin-dependent processes in our work, we calculate elastic cross sections using the Dirac equation which includes the possibility of spin flip during scattering by means of a so-called spin-flip scattering amplitude $g(\theta)$. The differential cross section is then expressed in terms of two scattering amplitudes f and g

$$\frac{d\sigma_e}{d\Omega} = |f(\theta)|^2 + |g(\theta)|^2, \tag{6}$$

where $f(\theta)$ is the direct scattering amplitude. The nonrelativistic limit corresponds to $g=0$, describing an electron whose spin direction is conserved during the scattering event. The ratio $|g|^2/(|f|^2+|g|^2)$ determines the probability for spin flip during the scattering process. The scattering amplitudes are independent of the azimuthal angle ϕ due to the spherical symmetry of the scattering potential.

For the calculation of differential and total elastic cross sections, we use the ELSEPA (elastic scattering of electrons and positrons by atoms) code of Salvat *et al.*[19] The Dirac equation for elastic scattering of an electron by a static central potential $V(r)$ approximated by a muffin-tin model potential is solved by partial-wave analysis. Electron densities are taken from multiconfiguration self-consistent Dirac-Fock calculations. Clearly, the high level of accuracy for differential cross sections for atoms cannot be reached in the solid environment, in particular, for energies below $\sim 10^2$ eV. However, integral cross sections determining λ_e should be sufficiently reliable. We have compared the obtained EMFP with calculations using an atomic potential (Fig. 3). The EMFP modeled by a muffin-tin potential is larger than for an atomic potential which is a consequence of the different r dependences of the potentials used. In the muffin-tin approximation, the deflection of trajectories is confined to impact parameters inside a sphere of the muffin-tin radius around the nucleus. The scattering cross section for large partial waves associated with impact parameters outside this sphere is smaller than in the case of a free atom target. This leads to a reduction of the differential cross section for small scattering angles, and subsequently, of the total cross section in solids compared to free atoms.

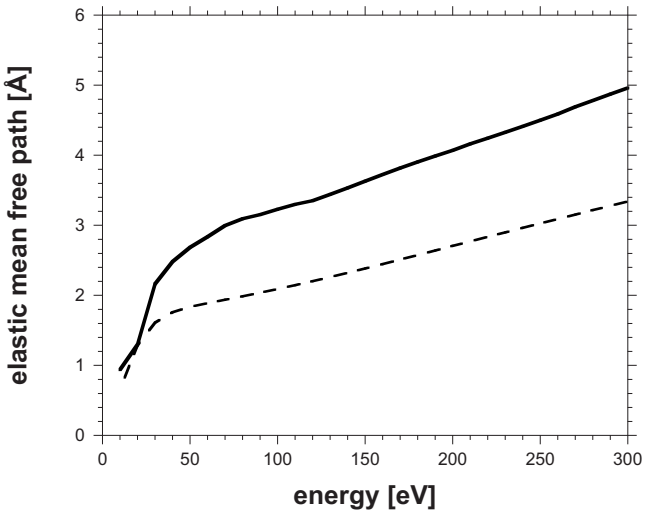

FIG. 3. Elastic mean free path λ_e for solid Fe represented by a muffin-tin potential (Ref. 19) (solid line) and for atomic Fe (dashed line).

D. Inelastic (bulk) scattering

We investigate both surface and bulk scattering processes. The cross section and corresponding inelastic mean free path (IMFP) $\lambda_{(\alpha=in)}$ in the bulk are calculated from the frequency and momentum dependent dielectric function $\epsilon(q,\omega)$. This quantity describes the response of the bulk electrons (plasmon and particle-hole pair excitations, inter- and intraband transitions) to an external perturbation with frequency ω and wave number q (see, e.g., Refs. 20 and 21). The inverse dielectric function $\epsilon^{-1}(q,\omega)$, or more precisely, the energy loss function $\mathrm{Im}\{-1/\epsilon(q,\omega)\}$ is related to the differential inverse mean free path as[22]

$$\frac{d^2\lambda_{in}^{-1}}{d\omega dq} = \frac{1}{\pi E q}\,\mathrm{Im}\left\{-\frac{1}{\epsilon(q,\omega)}\right\}\Theta[\omega_m(q)-\omega]. \tag{7}$$

Here, ω is the energy loss suffered by an electron with energy E, q is the transferred momentum, and the step function Θ assures momentum and energy conservation with $\omega_m(q) = \min[v_e^2/2 - E_F; v_e q - q^2/2]$. Here, v_e is the velocity of the scattered electron and E_F is the Fermi energy. The right hand side represents, up to a normalization factor, the collision kernel for inelastic scattering in the bulk. Integration of Eq. (7) over q yields the probability for an electron with energy E to lose the energy ω. Further integration over all possible energy losses (upper integration limit $\omega_{\max} = E - E_F$) gives the inverse inelastic mean free path as a function of the electron energy, $\lambda_{in}^{-1}(E)$, which determines the probability for an inelastic scattering event to take place. The angular distribution of the scattered electron follows from[20]

$$\frac{d\lambda_{in}^{-1}}{d\Omega} = \frac{1}{\pi^2}\int_0^\infty \frac{d\omega}{q^2}\sqrt{1-\frac{\omega}{E}}\,\mathrm{Im}\left\{-\frac{1}{\epsilon(q,\omega)}\right\}\Theta[E-E_F-\omega]. \tag{8}$$

For a given momentum (q) and energy transfer ω, Pauli blocking due to occupied final states is taken into account in Eq. (8).

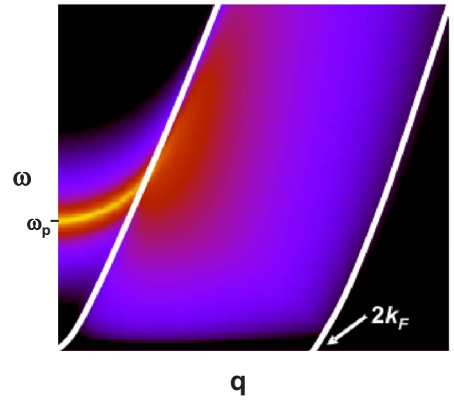

FIG. 4. (Color online) Momentum and energy dependent loss function $\mathrm{Im}\{-\epsilon(q,\omega)^{-1}\}$ of a free-electron gas (Al). The plasmon frequency ω_p coincides with the position of the maximum for $q=0$. The two lines demarcate the particle-hole pair continuum.

An analytic expression for $\epsilon(q,\omega)$ was first derived by Lindhard[23] for a free electron gas. It was later modified by Mermin[24] to account for the finite width of the plasmon peak. Figure 4 shows the loss function $\mathrm{Im}\{-\epsilon(q,\omega)^{-1}\}$ for the jellium-like metal Al, where a Mermin function was chosen for the dielectric function. For energies lower than the ionization energy of inner shells, the Mermin dielectric function is determined by the plasmon frequency $\omega_p = \sqrt{4\pi n}$ and the width γ of the plasmon peak, where n is the density of the free electron gas. Different contributions to inelastic loss can be distinguished in Fig. 4: the electron-hole pair continuum confined to the region between $\omega = q^2/2 \pm q k_F$ and the plasmon resonance peak starting at the plasmon frequency ω_p at $q=0$.

For transition metals with d electrons contributing to the conduction band structure (Fe, Au, Ni, etc.) the simple model of a quasi-free-electron gas breaks down. The optical data $\mathrm{Im}\{-\epsilon(q=0,\omega)^{-1}\}$ for Fe (see Fig. 5 and Ref. 25) feature a broad structure composed of the plasmon peak and convoluted by inter- and intraband transitions. Various models have been proposed to calculate $\epsilon(q,\omega)$ by extrapolation of $\epsilon(q=0,\omega)$ into the $q-\omega$ plane (e.g., Refs. 26–28). They have been successfully used to describe inelastic scattering of high-energy electrons. However, some of these models result in neglect of electron-hole pair excitations for very low energies ($\omega < 1$ a.u.), where this is the most important loss channel for electron trajectories down to the few-eV regime. The method of calculating $\epsilon(q,\omega)$ which we use in our work is very similar to one of those presented in Ref. 28. The starting point is a fit of the optical data $\mathrm{Im}(-\epsilon(\omega)^{-1})$ by a sum of Drude functions (Fig. 5). We then calculate the q and ω dependent loss function as a sum of several Drude functions,

$$\mathrm{Im}\left\{-\frac{1}{\epsilon(q,\omega)}\right\} = \sum_i A_i\,\mathrm{Im}\left\{-\frac{1}{\epsilon_i(q,\omega)}\right\}, \tag{9}$$

for each of which we employ the parametrized form[29]

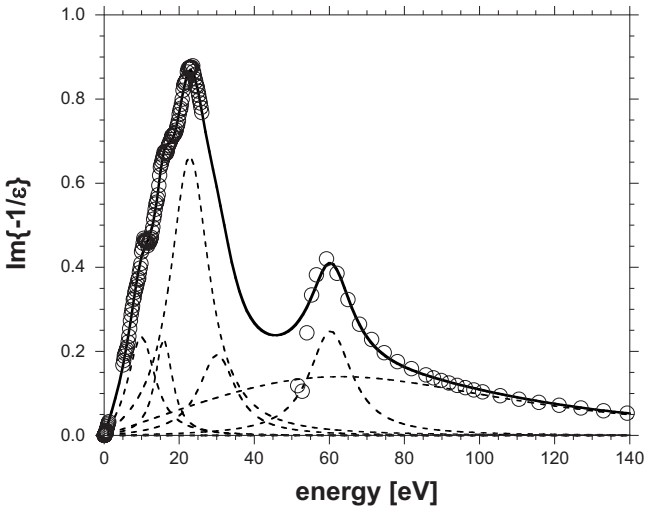

FIG. 5. Optical data of Fe (Ref. 25) (open circles), overall fit to $\mathrm{Im}(-\epsilon^{-1}(q=0,\omega))$ (solid line), and fit functions for the individual peaks (dashed lines).

$$\epsilon_i(q,\omega) = 1 + \frac{\omega_{p,i}^2}{s^2q^2 + q^4/4 - i\pi\omega s^2 q\Theta(x_1)\Theta(x_2)/2q_F - \omega[\omega + i\gamma_i]}, \tag{10}$$

where $s^2=3q_F^2/5$, according to the hydrodynamical model.[29] $\Theta(x_1)$ and $\Theta(x_2)$ are step functions with arguments $x_1=\omega - q^2/2+q_Fq$ and $x_2=q^2/2+q_Fq-\omega$ defining the regions of particle-hole pair creation and plasmon excitation in the $q-\omega$ plane (see Fig. 4). For each term, the "plasmon" frequency $\omega_{p,i}$, width γ_i, and weight A_i are determined by the fit to the optical data at $q=0$ and constrained by the Thomas-Reiche-Kuhn sum rule for the generalized oscillator strength,

$$\int_0^\infty d\omega\omega\,\mathrm{Im}\left\{-\frac{1}{\epsilon(q,\omega)}\right\} = 2\pi n. \tag{11}$$

The present method differs from that of Ref. 28 in the details of the fit function of Eq. (10) in which we preserve the distinction between regions of electron-hole pair creation and of collective excitations in the $q-\omega$ plane. We find only minor differences in the resulting numerical results for the collision kernel.

E. Surface excitations

As the penetration and escape depths of low-energy electrons are small, inelastic scattering processes due to surface excitations become increasingly important. They are treated here in the framework of the specular-reflection model, introduced by Ritchie and Marusak.[30] The surface dielectric function ϵ_s can be expressed in terms of the bulk dielectric function ϵ as[31]

$$\epsilon_s(Q,\omega,z) = \frac{Q}{\pi}\int dq_z \frac{e^{iq_zz}}{(Q^2+q_z^2)\epsilon(q,\omega)}, \tag{12}$$

where we use the notation $\vec{q}=(\vec{Q},q_z)$ with the z axis along the surface normal and with $z=0$ located at the surface. For the quasi-free-electron contribution, we can employ a jellium approximation within which $z=0$ corresponds to the jellium edge. In the following, we will extend Eq. (12) to d-band metals, the validity of which is an open question. Nevertheless, since our approach has the correct sum rules built into it, integral mean free paths should be reasonably well approximated. If we neglect dispersion along the z axis, i.e., $\epsilon(q,\omega)\simeq\epsilon(Q,\omega)$, the surface dielectric function can be approximated by

$$\epsilon_s(Q,\omega,z) \simeq \epsilon(Q,\omega)^{-1}e^{-Q|z|} \tag{13}$$

and the inverse surface inelastic mean free path $\lambda_{(\alpha=s)}^{-1}$ is given by[22]

$$\frac{d^2\lambda_s^{-1}}{dQd\omega} = \frac{2e^{-2Q|z|}}{v_\parallel\pi\sqrt{Q^2v_\parallel^2 - \left(\omega+\frac{Q^2}{2}\right)^2}} \times \mathrm{Im}\left\{\frac{\epsilon(Q,\omega)-1}{\epsilon(Q,\omega)+1}\right\}\Theta[\omega_m(Q)-\omega], \tag{14}$$

where $\omega_m(Q)=\min[v_\parallel^2/2-E_F;v_\parallel Q-Q^2/2]$ and $v_\parallel$ is the velocity component parallel to the surface. Although Eq. (13) was derived for electrons moving parallel to the surface,[30] it is a reasonable approximation also for electrons with $q_z\neq0$ for the energies and the dielectric properties of the material considered in our work. We verified the validity of Eq. (13) by numerical calculations at eight different distances z between the jellium edge and $z=-20$. For all z, the relative error of Eq. (13) lies below 10%; only for $z=0$ is the maximum error about 20%. λ_s^{-1} has its maximum at the surface and decreases with increasing distance to the jellium edge. The energy dependence of the bulk inelastic MFP λ_{in} and of the surface MFP at $z=0$ (Fig. 6) clearly indicate that surface inelastic processes dominate over bulk processes near the surface over a wide range of energies.

For reasons of computational efficiency for the Monte Carlo simulation, the z dependence resulting from Eq. (14) was fitted to the analytic formula $\lambda_s(z)=\lambda_s(0)(1+a|z|^b)$ with energy-dependent parameters $a(E)$ and $b(E)$ which were found to be $a=1.04-0.008E$ and $b=2.08-0.24\log E$ for $E>E_{min}$ and $a=0.19+0.54E$ and $b=1.96-\exp(-7.8(E-0.4))$ for $E<E_{min}$, where $E_{min}=1.6$ a.u. (43 eV) corresponds to the minimum in λ_s (see Fig. 6).

As the generalized oscillator strength is shifted from the bulk to the surface response function, we incorporate the z dependence into the bulk λ_{in} near the surface such that (i) for large distances from the surface, λ_{in}^{-1} asymptotically tends to its bulk value [i.e., Eq. (7)] and (ii) λ_{in}^{-1} tends to zero at the surface. In Ref. 22, it was proposed to include the z dependent factor $(1-e^{-2Q|z|})$ in Eq. (7) which assures that these two criteria are satisfied. We adopted this choice for our calculations.

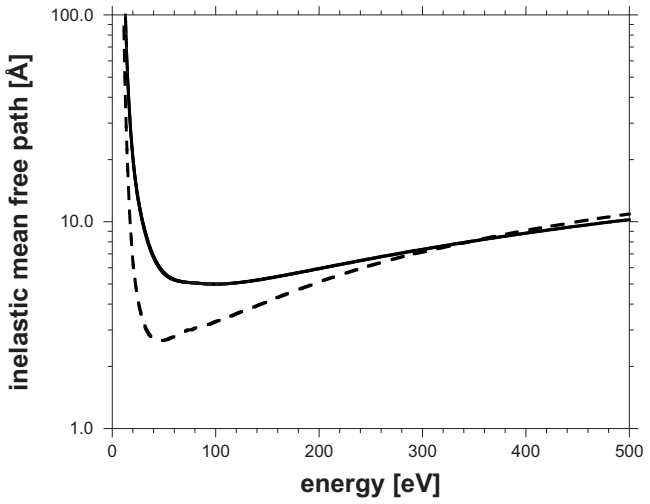

FIG. 6. Bulk $[\lambda_{in}(-\infty)$, solid line] and surface $[\lambda_s(0)$, dashed line] inelastic mean free paths for Fe (see text).

F. Spin effects in electron scattering

Spin-dependent effects can contribute to both inelastic and elastic scattering. Spin dependence of the latter is parametrized by the Sherman function $S(\theta)$,[32]

$$S(\theta)=i\,\frac{f(\theta)g^*(\theta)-f^*(\theta)g(\theta)}{|f(\theta)|^2+|g(\theta)|^2}, \tag{15}$$

which is a measure for the asymmetry between spin-up and spin-down cross sections. Measurement of electron polarization in Mott detectors exploits the broad maximum (full width at half maximum in the range of 50°–100°) of the Sherman function for electron energies of several tens of keV. For the material and energies considered in our work, however, $S(\theta)$ features very small values over the whole range of scattering angles and renders elastic scattering effectively spin independent. Consequently, spin polarization of low-energy electron beams in magnetized iron is dominated by inelastic scattering events. We treat two processes which are expected to control the polarization of emitted electrons, schematically depicted in Fig. 7. Magnetization of the band structure is characterized by a shift of the minority SDOS relative to the majority SDOS by the exchange splitting Δ. The occupation of majority and minority states is unbalanced. Spin-up electrons are, therefore, more likely to be excited and emitted in an inelastic collision (left panel of Fig. 7). On average, secondary electrons generated in a collision cascade by primary electrons with energies large compared to E_F should reflect the mean polarization $\bar{P}$ of the target conduction band, which in the case of iron is $\bar{P}\approx 35\%$ according to the band structure calculations (Sec. II B).

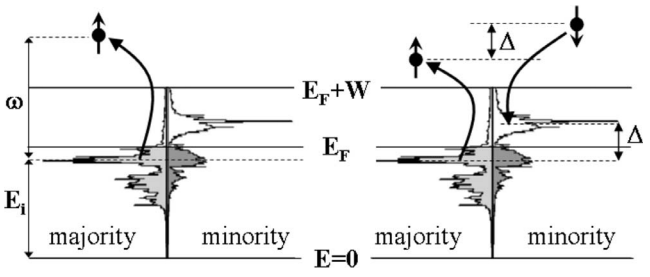

FIG. 7. Illustration of spin-dependent scattering processes for the bulk SDOS of Fe. Left panel: A secondary electron with initial energy E_i is excited to a continuum state of energy $E_i+\omega$. On the average, more majority than minority electrons are emitted due to the positive polarization of the occupied states. Right panel: Spin-filter effect due to Stoner excitations controlled by the unoccupied part of the spin densities of states (see text).

The second process is the so-called Stoner excitation (right panel in Fig. 7). It results from the unoccupied SDOS which is available for final states of electron-electron scattering processes. An electron with minority spin has access to a larger number of final states in an inelastic collision accompanied by energy loss. Since the number of available final states determines, by way of Fermi's golden rule, the collision probability, the collision rate of minority spin electrons is enhanced relative to that of majority spin electrons. The excess energy is transferred to an electron from the occupied part of the conduction band which is predominantly of majority spin, so that this process appears as inelastic scattering accompanied by a spin flip of the electron even though no explicitly spin-dependent interactions enter the transition amplitude. As the maxima of the two spin density distributions are separated by the energy $\Delta\approx 2.5$ eV, a characteristic energy loss of $\omega\simeq\Delta$ connected to a change of polarization is observed in the experiment.[33]

The asymmetry between unoccupied spin-up and spin-down states results in a spin-dependent IMFP. Minority electrons are scattered more often than majority electrons and, consequently, have a shorter mean free path. The asymmetry between the spin-up and spin-down IMFPs decreases with increasing primary energy due to the decreasing probability of the electron to access a final state below the vacuum level $E_v=E_F+W$, where W is the work function of the target. If the final state of the scattered electron lies above E_v, there are as many free final states for majority as for minority electrons. Only below E_v does a spin dependence of available final states become significant. We, therefore, separate inelastic scattering in collisions with final states above and below E_v. Accordingly, we split the integration of $d\lambda_{in}^{-1}/d\omega$ over the energy loss ω as

$$\begin{aligned}\lambda_{in}^{-1}&=\int_0^{E-E_F}\frac{d\lambda_{in}^{-1}}{d\omega}d\omega\\&=\int_0^{E-E_F-W}\frac{d\lambda_{in}^{-1}}{d\omega}d\omega+\int_{E-E_F-W}^{E-E_F}\frac{d\lambda_{in}^{-1}}{d\omega}d\omega=\lambda_{>E_v}^{-1}+\lambda_{<E_v}^{-1}.\end{aligned} \tag{16}$$

The first integral corresponds to spin-independent scattering processes with final projectile state above the vacuum level, while the second integral describes scattering to states with energies $E_F<E<E_v$. Up to this point, the latter contribution is also spin independent, as the construction of $\epsilon(q,\omega)$ is based on spin-independent photoabsorption spectra. To ac-

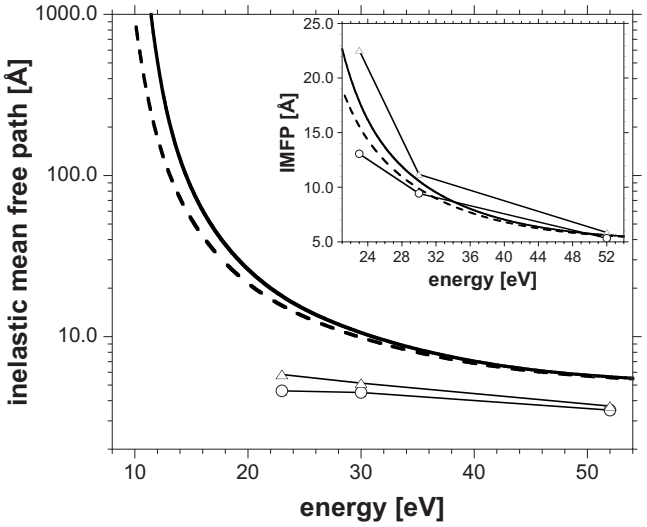

FIG. 8. Spin-dependent inelastic mean free paths $\lambda_{in,\uparrow}$ (solid line) and $\lambda_{in,\downarrow}$ (dashed line). The asymmetry between $\lambda_{in,\uparrow}$ and $\lambda_{in,\downarrow}$ due to Stoner excitations increases with decreasing energy. Experimental results for $\lambda_{\uparrow(\downarrow)}$ which include elastic scattering (Ref. 34) are also shown (open triangles: spin-up; open circles: spin-down, lines are to guide the eyes). Inset: Comparison with the experimental data after subtraction of estimated elastic contributions.

count for the magnetization of the target, we calculate the number of unoccupied (ferromagnetic) spin-up ($N_\uparrow$) and spin-down states ($N_\downarrow$) and weight the spin-independent (paramagnetic) $\lambda^{-1}_{<E_v}$ by the ratio of majority (minority) to paramagnetic states (denoted by N_0):

$$\lambda^{-1}_{<E_v,\uparrow} = \lambda^{-1}_{<E_v}\frac{N_\uparrow}{N_0},$$

$$\lambda^{-1}_{<E_v,\downarrow} = \lambda^{-1}_{<E_v}\frac{N_\downarrow}{N_0}, \tag{17}$$

where $N_0=N_\uparrow+N_\downarrow$ is the total number of unoccupied states. Using the calculated SDOS for iron (Fig. 2), we find the ratios $N_{\uparrow(\downarrow)}/N_0$ to be 0.172 for spin up and 0.828 for spin down. The resulting spin-dependent total IMFP (Fig. 8) is given by

$$\lambda^{-1}_{in\uparrow(\downarrow)} = \lambda^{-1}_{>E_v} + \lambda^{-1}_{<E_v,\uparrow(\downarrow)}. \tag{18}$$

Increasingly large differences between $\lambda_{in\uparrow}$ and $\lambda_{in\downarrow}$ at small energies lead to the spin-filter effect. Experimental data for a spin-dependent IMFP, denoted by $\lambda_{expt\uparrow(\downarrow)}$ in the following (Ref. 34, also shown in Fig. 8), contain largely spin-independent elastic contributions. For a comparison with the present $\lambda_{in\uparrow(\downarrow)}$, we subtract the elastic contribution by setting $\lambda^{-1}_{expt\uparrow(\downarrow)}=\lambda^{-1}_{in\uparrow(\downarrow)}+\lambda'^{-1}_e$, where the prime indicates that the experimental λ'_e includes only part of the elastic scattering events due to the restricted scattering geometry. The corrected experimental data are in fair agreement with the calculated asymmetry between $\lambda_{in\uparrow}$ and $\lambda_{in\downarrow}$ considering the large uncertainty of the data reduction.

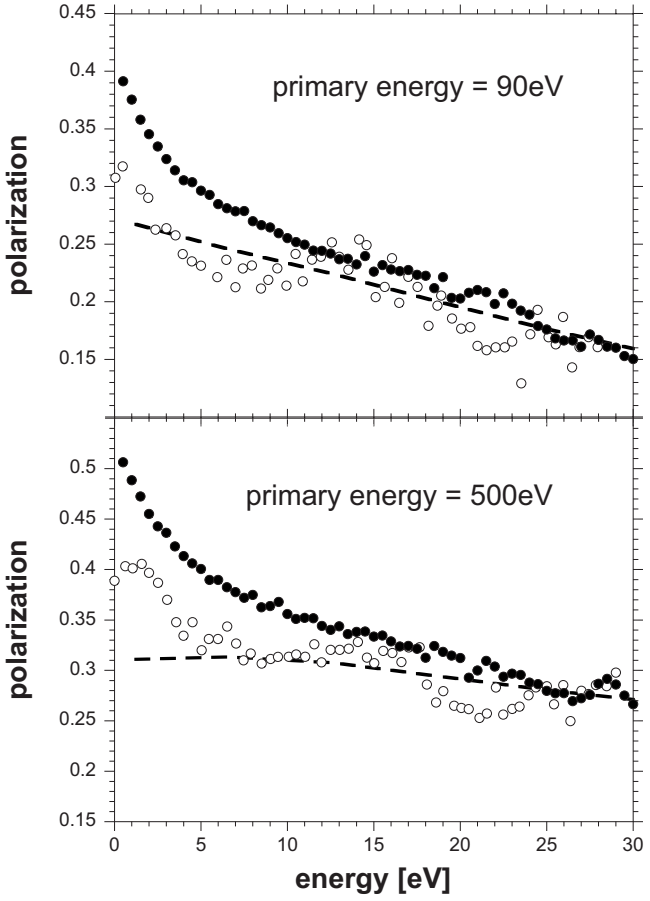

FIG. 9. Spin polarization of emitted electrons from a magnetized Fe(110) surface bombarded with 90 and 500 eV unpolarized electrons. Open circles: experimental results (Ref. 3); full circles: present simulation. The dashed lines indicate the simulated polarization neglecting Stoner excitations.

The present analysis of spin-dependent scattering relies on the SDOS of the bulk. For low-energy electron scattering, the surface region becomes increasingly important. To include the variation of the magnetized band structure with the distance from the topmost layer, detailed knowledge of the local SDOS near the surface would be required. Currently, available data[35] are too sparse and rapidly changing as a function of z. We plan to include surface dependent spin-polarized scattering when new data on the local SDOS will become available.

III. APPLICATION TO Fe

We have implemented our CTT for iron and applied it to the experiments of Kirschner and Koike,[3] in which unpolarized electron beams were scattered at a magnetized Fe surface. We compare measured spin polarization data of emitted secondary electrons from Fe(110) (Ref. 3) with our calculations for primary energies of 90 and 500 eV (Fig. 9). Two trends are observed in the experiment and reproduced by our calculation: (1) the polarization of low-energy electrons increases with increasing primary energy and (2) the largest polarization values are reached at emission energies below

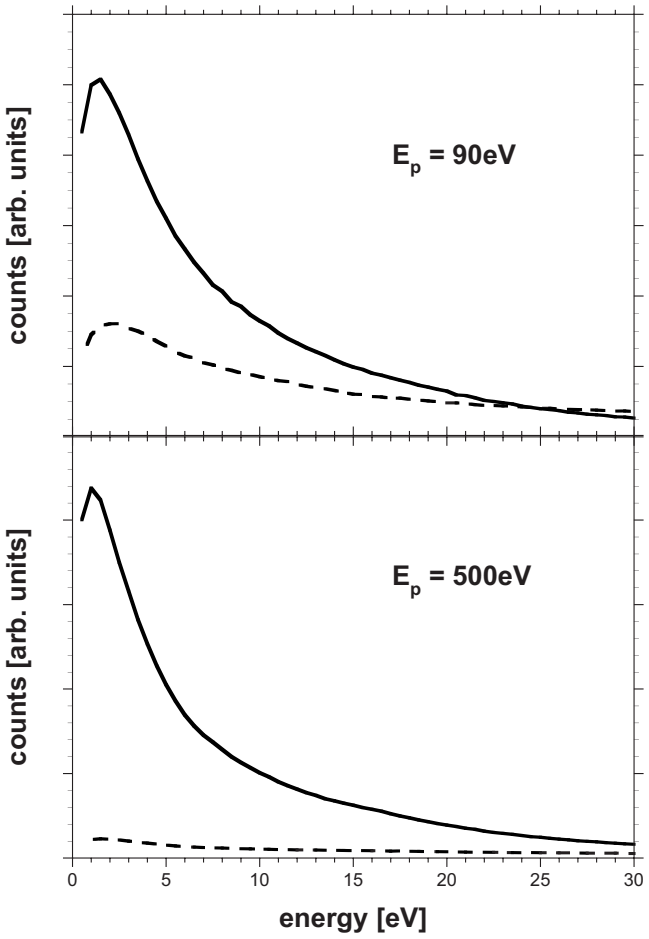

FIG. 10. Emission spectrum after impact of 90 eV (upper panel) and 500 eV (lower panel) primary electrons on Fe, separated into contributions of secondary electrons (solid lines) and backscattered primaries (dashed lines).

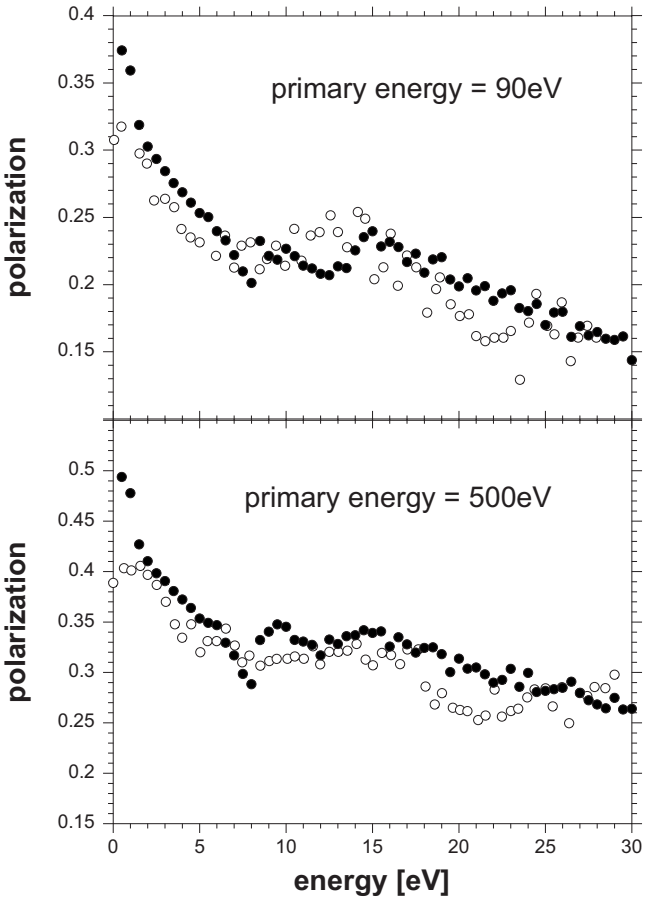

FIG. 11. Notation as in Fig. 9 but including the additional polarization contribution due to plasmon decay near the Fermi edge (see text).

5 eV. The latter feature is quite remarkable as the mean polarization of the occupied magnetic band structure does not exceed ~35%. It is obviously the result of a high degree of spin selectivity due to the spin-filter effect of Stoner excitations. A much reduced degree of polarization would result by neglecting Stoner excitations (see Fig. 9).

Our simulation can also quantitatively account for the increase of the spin polarization with increasing primary electron energy. This is to a large degree due to the increased statistical weight of spin-polarized secondary electrons relative to that of the unpolarized primary electrons. The latter is the result of two trends. At higher energies, backscattering into vacuum of the primary electrons is suppressed as the penetration depth increases and the number of low-energy secondary electrons generated by primary electrons increases with energy. The decreasing importance of backscattered primaries with increasing impact energy is clearly visible in Fig. 10. Saturation will be reached when the secondary electron cascade has fully evolved and the number of backscattered primaries (N_p) becomes negligible, so that $N_s+N_p \simeq N_s$, where N_s is the number of emitted secondaries. In the absence of explicitly spin-dependent interactions, backscattered primary electrons keep their original polarization $P_p=0$, while secondary electrons are emitted with the average polarization of the conduction band $P_s=\bar{P}\simeq 35\%$. The polarization of emitted electrons, therefore, lies between 0 and 35% depending on the ratio $N_s/(N_p+N_s)$ as long as Stoner excitations are not taken into account (dashed lines in Fig. 9). Polarization values above $\bar{P}$ originate from Stoner excitations. The polarization values at very low energies depend on the asymmetry between $\lambda_{in\uparrow}$ and $\lambda_{in\downarrow}$. Along with the saturation for the weight of secondaries, a saturation must also appear for the polarization at high primary energies, which has been observed in experiment.[3] For $E_p=500$ eV, backscattered primary electrons are still visible in the low-energy spectrum (Fig. 10), so that we are not yet in the saturation regime, which was experimentally determined to be at about $E_p=1$ keV.[3]

Overall, experiment and simulation are in excellent agreement. There is, however, a systematic discrepancy at emission energies between about 10 and 20 eV visible for both primary energies $E_p=90$ eV and $E_p=500$ eV. The origin of this "hump" was experimentally investigated by additional measurements on oxygen exposed Fe. Since the hump between 10 and 20 eV was still visible, it was concluded that this feature is related to bulk and not to surface excitations. As this energy window coincides with the electron energy expected for plasmon decay ($\omega_p \approx 15$ eV) into particle-hole

pair excitations, it is suggestive to relate this feature to the decay of volume plasmons. In order to explain the enhancement of the polarization, a spin-selective decay mode has to be invoked. We, therefore, introduce the plausible hypothesis that the decay of plasmons involves electrons preferentially near the Fermi edge, where the intrinsic momentum distribution (Compton profile) minimizes the required momentum transfer for the decay to take place. To test our hypothesis, we have slightly increased the probability to excite secondary electrons from a narrow window ($E_F - 0.3$ eV $< E < E_F$) around the Fermi edge when created via plasmon decay ($\omega \approx \omega_p$). Assuming a fixed value of 0.7 for the probability that the plasmon decays via electron emission from this energy window, the polarization distribution is, indeed, in better agreement with the experiment (Fig. 11). However, a more detailed study of the plasmon decay dynamics is required to validate this hypothesis.

IV. CONCLUSIONS

We have presented a simulation of low-energy electron emission by moderately energetic electrons within the framework of the classical transport theory.[15] The spin degree of freedom was included by following subensembles of spin-up and spin-down electrons. The simulation involves state-of-the-art band structure calculations of both occupied and unoccupied states. Trajectories are determined by a sequence of stochastic elastic and inelastic scattering events. The latter include interactions with the target conduction band (creation of electron-hole pairs, excitation of plasmons, inter- and intraband transitions), excitation of core electrons, and Stoner excitations, a spin-flipping process caused by the excess of unoccupied states in the minority spin density of states just above the Fermi edge. Creation of surface excitations is also included in our simulation as an allowed energy loss channel. We have applied the present theory to the polarized electron spectroscopy data for Fe by Kirschner and Koike.[3] Overall, we find good agreement with the experimental data.

Future extensions will address electron emission in (multiply charged) ion-surface scattering, where the experimental spectra are a convolution of above- and sub-surface processes (potential and kinetic emission, production of secondary electrons). Our simulations will allow for a separation of the different contributions to the spectra and are expected to yield a detailed interpretation of the experimental data.

ACKNOWLEDGMENTS

This work was supported by the Austrian Fonds zur Förderung der Wissenschaftlichen Forschung (FWF Austria) under Project No. P17449-N02, by EU under Contract No. HPRI-CT-2005-026015, the Hungarian Scientific Research Fund OTKA No. T046095 and No. T046454, the grant "Bolyai" from the Hungarian Academy of Sciences, and the Stiftung Aktion Österreich-Ungarn No. 67öu3.

[1] R. L. Long, Jr., V. W. Hughes, J. S. Greenberg, I. Ames, and R. L. Christensen, Phys. Rev. **138**, A1630 (1965).
[2] G. Busch, M. Campagna, and H. C. Siegmann, Phys. Rev. B **4**, 746 (1971).
[3] J. Kirschner and K. Koike, Surf. Sci. **273**, 147 (1992).
[4] M. Unipan, D. F. A. Winters, A. Robin, R. Morgenstern, and R. Hoekstra, Nucl. Instrum. Methods Phys. Res. B **230**, 356 (2005).
[5] J. C. Lancaster, F. J. Kontur, G. K. Walters, and F. B. Dunning, Phys. Rev. B **67**, 115413 (2003).
[6] J. Berakdar and H. Klar, Phys. Rev. Lett. **69**, 1175 (1992).
[7] J. Kessler, *Polarized Electrons*, 2nd ed. (Springer, Berlin, 1985).
[8] N. Berdunov, S. Murphy, G. Mariotto, and I. V. Shvets, Phys. Rev. Lett. **93**, 057201 (2004).
[9] J. A. D. Matthew, Phys. Rev. B **25**, 3326 (1982).
[10] D. R. Penn, S. P. Apell, and S. M. Girvin, Phys. Rev. Lett. **55**, 518 (1985).
[11] M. Yasuda, K. Tamura, H. Kawata, and K. Murata, J. Phys. D **34**, 1955 (2001).
[12] Xia Sun and Zejun Ding, J. Phys. D **38**, 456 (2005).
[13] J. Glazer and E. Tosatti, Solid State Commun. **52**, 905 (1984).
[14] H. Hopster, R. Raue, and R. Clauberg, Phys. Rev. Lett. **53**, 695 (1984).
[15] J. Burgdörfer and J. Gibbons, Phys. Rev. A **42**, 1206 (1990); J. Burgdörfer, in *Physics of Electronic and Atomic Collisions*, edited by A. Dalgarno *et al.*, AIP Conf. Proc. No. 205 (AIP, New York, 1990), p. 476; C. Deiss, N. Rohringer, J. Burgdörfer, E. Lamour, C. Prigent, J. P. Rozet, and D. Vernhet, Phys. Rev. Lett. **96**, 013203 (2006).
[16] J. Burgdörfer and C. Lemell, *Theoretical Concepts and Methods for Electron Emission from Solid Surfaces*, Springer Tracts in Modern Physics Vol. 225 (Springer, Berlin, 2007).
[17] M. Weinert, E. Wimmer, and A. J. Freeman, Phys. Rev. B **26**, 4571 (1982); H. J. F. Jansen and A. J. Freeman, *ibid.* **30**, 561 (1984).
[18] J. P. Perdew, K. Burke, and M. Ernzerhof, Phys. Rev. Lett. **77**, 3865 (1996).
[19] F. Salvat, A. Jablonski, and C. Powell, Comput. Phys. Commun. **165**, 157 (2005).
[20] Z. J. Ding and R. Shimizu, Surf. Sci. **222**, 313 (1989).
[21] K. Tőkési, D. Varga, L. Köver, and T. Mukoyama, J. Electron Spectrosc. Relat. Phenom. **76**, 427 (1995).
[22] C. O. Reinhold and J. Burgdörfer, Phys. Rev. A **55**, 450 (1997).
[23] J. Lindhard, K. Dan. Vidensk. Selsk. Mat. Fys. Medd. **28**, 1 (1954).
[24] N. D. Mermin, Phys. Rev. B **1**, 2362 (1970).
[25] *Handbook of Optical Constants of Solids 2*, edited by E. D. Palik, (Academic, New York, 1991).
[26] C. J. Powell, Surf. Sci. **44**, 29 (1974).
[27] D. R. Penn, Phys. Rev. B **35**, 482 (1987).
[28] K. Tőkési, L. Wirtz, C. Lemell, and J. Burgdörfer, Phys. Rev. A **64**, 042902 (2001).
[29] K. Tőkési, X.-M. Tong, C. Lemell, and J. Burgdörfer, Phys. Rev. A **72**, 022901 (2005).

[30] R. H. Ritchie and A. L. Marusak, Surf. Sci. **4**, 234 (1966).
[31] F. J. García de Abajo and P. M. Echenique, Phys. Rev. B **46**, 2663 (1992).
[32] J. Kessler, Rev. Mod. Phys. **41**, 3 (1969).
[33] M. S. Hammond, G. Fahsold, and J. Kirschner, Phys. Rev. B **45**, 6131 (1992).
[34] D. P. Pappas, K.-P. Kämper, B. P. Miller, H. Hopster, D. E. Fowler, C. R. Brundle, A. C. Luntz, and Z.-X. Shen, Phys. Rev. Lett. **66**, 504 (1991).
[35] J. A. Stroscio, D. T. Pierce, A. Davies, R. J. Celotta, and M. Weinert, Phys. Rev. Lett. **75**, 2960 (1995).